Microporous and Mesoporous Materials 218 (2015) 101–111

Contents lists available at ScienceDirect

Microporous and Mesoporous Materials

journal homepage: www.elsevier.com/locate/micromeso

Modification of mesoporous silica magnetite nanoparticles by 3-aminopropyltriethoxysilane for the removal of Cr(VI) from aqueous solution

Samira Hozhabr Araghi [a], Mohammad H. Entezari [a, b, *], Mahmoud Chamsaz [c]

[a] Sonochemical Research Center, Department of Chemistry, Faculty of Science, Ferdowsi University of Mashhad, 91779, Mashhad, Iran
[b] Environmental Chemistry Research Center, Department of Chemistry, Faculty of Science, Ferdowsi University of Mashhad, 91779, Mashhad, Iran
[c] Department of Chemistry, Faculty of Science, Ferdowsi University of Mashhad, 91779, Mashhad, Iran

ARTICLE INFO

Article history:
Received 25 May 2015
Received in revised form
8 July 2015
Accepted 8 July 2015
Available online 17 July 2015

Keywords:
Mesoporous silica magnetite NPs
Core-shell structure
Cr(VI) removal
Adsorption mechanism
Quantum mechanics calculations

ABSTRACT

Silica magnetite nanoparticles (S-MNPs) as core were embedded in mesoporous silica shells by using cetyltrimethylammonium bromide (CTAB) as a surfactant. Then, the resultant mesoporous silica-magnetite nanoparticles (M-S-MNPs) were modified with 3-aminopropyltriethoxysilane (APTES) as a coupling agent in dry hexane solvent. APTES-grafted mesoporous silica magnetite nanoparticles (A-M-S-MNPs) were characterized by XRD, FTIR spectroscopy, EDX, TEM, elemental analysis, TGA/DTA technique. Results demonstrate that the obtained A-M-S-MNPs were nearly spherical in shape with 25 nm thick mesoporous silica shell. The adsorption behavior of the nanocomposite was examined in removing of Cr(VI) ion with concentrations 20, 30 and 50 mg/L at optimum pH level of 2. In this study a pH swing adsorption was observed too. The adsorption kinetic data were modeled using pseudo-second-order kinetics and intraparticle diffusion equations. The obtained results for intraparticle diffusion model show that the adsorption mechanisms are different in low and in high concentrations of Cr(VI) ion. According to the parameters of the Langmuir isotherm, the maximum adsorption capacity (q_m) of A-M-S-MNPs for Cr(VI) increases as the temperature rises from 298 to 318 K. For better understanding of adsorption mechanism, quantum mechanical methods were applied. The results indicate that the electrostatic and hydrogen bond interactions between surface functional groups and $HCrO_4^-$ ions have an important role in adsorption process. The easy separation from aqueous solution by an external magnetic field, rapid adsorption, regeneration, and reusability of A-M-S-MNPs are interesting points as an effective adsorbent for the removal of Cr(VI) ions.

1. Introduction

In recent years, discharge of industrial wastewater containing heavy metal ions in nature has become one of the main environmental subjects due to the adverse effects of these ions on ecosystem and human health. Among the heavy metal ions, Cr(VI) with its wide application in different industries such as electroplating, leather tanning, and pigment industry has been extremely considered [1,2]. Depending on pH and redox conditions, chromium exists generally in two oxidation states Cr(VI) and Cr(III) in the aqueous solutions [3]. Cr(VI) has more mobility and solubility than another specie. Cr(III) is considered as a necessary element for controlling of glucose, lipid and protein metabolism in the human and animal body. While Cr(VI) is very dangerous to living organism due to its toxicity, mutagenic and carcinogenic properties [4,5]. Therefore, efficient removal of Cr(VI) from wastewaters is an important issue. Various treatment techniques have been used for the removal Cr(VI) from aqueous solutions such as ion exchange, precipitation, reverse osmosis and membrane processes. These methods have major drawbacks including incomplete metal removal, high reagents or energy requirements and generation of toxic sludge or secondary waste [6,7]. Therefore, the adsorption process as a high efficiency and low cost method can be used for the treatment of wastewater containing heavy metals [8,9].

Recently magnetite nanoparticles (MNPs) are applied as useful adsorbents for cleanup of environmental contaminants because of

* Corresponding author. Sonochemical Research Center, Environmental Chemistry Research Center, Department of Chemistry, Faculty of Science, Ferdowsi University of Mashhad, 91779, Mashhad, Iran.
E-mail addresses: entezari@um.ac.ir, moh_entezari@yahoo.com (M.H. Entezari).

http://dx.doi.org/10.1016/j.micromeso.2015.07.008
1387-1811/

their high surface area, easy separation from aqueous media under external magnetic fields [10,11]. Despite these positive features, MNPs are associated with several deficiencies such as aggregation, oxidation in air and instability under acidic conditions. For reduction of these undesirable features, bare MNPs are embedded into a host matrix [12]. Since mesoporous structures have large surface area, tunable pore size and well-defined pore structures [13,14], it is expected that suitable combination of MNPs and mesoporous structures as host matrix could make nanocomposites with novel properties. The mesoporous silica structure as a proper candidate not only provide large accessible pore volume for adsorption of toxic compounds in water but also are modified easily by a wide range of functional groups for high adsorption capacity and selectivity [15,16]. The 3-aminopropyltriethoxysilan (APTES) is the most common organosilane that is used for functionalization of silica surfaces [17]. Amino group in this molecule has a bi-functional nature and could adsorb anionic and cationic pollutants [18–20]. In general, two strategies post-synthesis or post-grafting and direct synthesis or co-condensation are applied for the modification of silica surfaces [21]. In post-synthesis method, modification performs by covalent bonding of organosilanes species with silanol groups on silica surfaces. Since in this method, the synthesis of silica surface and functionalization carry out in two separated steps, controlling of pore size, particle size and particle morphology becomes more straight forward than co-condensation method. Modification of silica surface with organosilanes is usually carried out by refluxing in dry organic solvent [22].

In this work, A-M-S-MNPs were synthesized by embedding of S-MNPs in a mesoporous silica shell and then grafting of APTES molecules was performed by post-synthesis method in dry hexane. Size, morphology, nature of pores and amount of APTES loading for this nanocomposite were determined by different characterization methods. A-M-S-MNPs were applied as a novel adsorbent for the fast and efficient removal of Cr(VI) from aqueous solution. Effect of pH values, initial concentration, adsorption kinetics, thermodynamics parameters, ionic strength, regeneration and reusability on the removal of Cr(VI) have been studied. Determination of effective interactions between adsorbent and adsorbate was investigated by quantum mechanics calculations.

2. Experimental

2.1. Materials

All reagents were of analytical grade and used as received. Iron (II) sulfate heptahydrate ($FeSO_4 \cdot 7H_2O$), sodium hydroxide (NaOH), potassium nitrate (KNO_3), potassium dichromate ($K_2Cr_2O_7$), sodium chloride (NaCl), ammonium nitrate (NH_4NO_3), 4-nitrobenzaldehyde, 1,5-diphenylcarbazide, ninhydrin, acetic acid (CH_3CO_2H), sulfuric acid (H_2SO_4, 98%), (H_3PO_4, 85%), absolute ethanol, acetone, tetraethyl orthosilicate (TEOS, >98%), 3-aminpropyltriethoxysilane (APTES, >98%), hexane (96%) and concentrated ammonia solution (25%), were purchased from Merck. Cetyltrimethylammonium bromide (CTAB), hydrochloric acid (HCl, 37%), were purchased from Sigma Aldrich. The de-ionized water was used in the synthesis and preparation of solutions.

2.2. Synthesis of adsorbent

The synthesis of MNPs were performed according to the reported procedure [23]. Briefly, two different solutions were prepared as follows: (1) dissolving of desired amount of NaOH and KNO_3 in 180 mL deionized water so that the final concentration of NaOH and KNO_3 reach to 7×10^{-2} and 0.1 M respectively, (2) dissolving of desired amount of $FeSO_4 \cdot 7H_2O$ in 20 mL 10^{-2} M H_2SO_4 to obtain a solution with concentration of 7.4×10^{-2} M. After preparation the solutions, argon gas was bubbled into the solutions for 2 h. Then, solution (2) was added dropwise to basic solution under stirring. When the precipitation was completed, the container was placed in oil bath (90 °C) without stirring for 24 h. The obtained product was collected by a magnet and washed with deionized water.

To prepare of silica coated MNPs, 0.4 g of MNPs was added to a mixture containing 25 mL deionized water, 100 mL ethanol and 2 mL concentrated ammonia (25%) in a flask. The mixture was stirred vigorously for 30 min at 35 °C. Afterward, 0.3 mL of TEOS was added per hour until the total volume of TEOS reach to 2 mL. Finally, the resulting S-MNPs were collected by magnetic separation and washed with deionized water and ethanol several times.

To synthesize of M-S-MNPs, a desired amount of S-MNPs was dispersed in a mixture containing of deionized water, ethanol, concentrated ammonia and 1 g CTAB. After homogenization of the mixture by mechanical stirrer, 4 mL of TEOS was added dropwise to the mixture and the reaction was continued for 6 h at 30 °C. The product was washed with ethanol and water. For removing of surfactant and formation of mesoporous structure, two methods of calcination and solvent extraction are frequently used. In calcination method, some silanol groups are dehydroxylated at high temperature and then few numbers of APTES molecules can be grafted to the silica surface. Therefore, solvent extraction with ethanol and ammonium nitrate was selected as an appropriate method for removing of CTAB. 1.5 g of the sample was refluxed at 90 °C for 1 h in solution including 1 g ammonium nitrate in 80 mL ethanol. To complete extraction of CTAB, the procedure was repeated several times [24].

Since the silylating agent is polymerized in the presence of small amount of water, the APTES bottle was opened in a dry Ar-purged glove box and amino-functionalization experiment was performed under inert atmosphere by anhydrous hexane solvent. In addition, the silica surface adsorbs the humidity and for the desorption of physisorbed water, the M-S-MNPs was heated at 180 °C for 3 h [25]. Then M-S-MNPs were placed in a 100 mL three-necked flask containing 30 mL of dry hexane. After Ar purge in solution for 1 h, 6 mmol APTES was added into the flask. Then the mixture reaction was heated under reflux at 68 °C for 24 h. In order to remove the unreacted APTES molecules, the resultant A-M-S-MNPs were washed by dry hexane three times.

2.3. Characterization methods

The XRD patterns of samples were obtained at room temperature using a X'Pert Pro MPD X-ray powder diffraction (Netherlands) with Cu Kα radiation (λ = 0.154 nm). The unite cell parameter (a_0) could be calculated from d_{100} value by the following equation.

$$a_0 = \frac{2d_{100}}{3^{1/2}} \quad (1)$$

Fourier transform infrared (FTIR) spectra of samples were recorded by Thermo Nicolet Avatar 370 FTIR spectrometer using the KBr disc technique. The spectra were collected in the 400–4000 cm^{-1} range. The TEM image was taken on a Philips CM120 transmission electron microscope. The energy dispersive X-ray (EDX) was obtained on a LEO 1450VP scanning electron microscope (SEM) coupled with an Oxford 7353 EDX at acceleration voltage 20 and 5 kV. Thermogravimetric (TGA) and differential thermal (DTA) analysis were measured using a Shimadzu DTA/TGA-50 with heating rate of 20 °C/min under a nitrogen atmosphere. Carbon, nitrogen, hydrogen and oxygen contents were determined with a VARIAN elemental analyzer model CH 7 A (Germany). The

concentration of Cr(VI) in aqueous solutions was determined by UV–vis spectrophotometer (Unico 2800) in the range 400–700 nm.

2.4. Adsorption experiments

Standard solutions of Cr(VI) in different concentrations are prepared from dissolving of $K_2Cr_2O_7$ in deionized water. The HCl solution was used to adjust pH solutions to 2. In all adsorption experiments, 0.035 g of A-M-S-MNPs is placed in a double-walled glass jar containing 25 mL of Cr(VI) solution and stirred at different interval times. It should be noted that except the series of experiments related to the isotherm study, the others are performed at room temperature. To determine the residual concentration of Cr(VI) in the solution, the colorimetric was applied. Briefly, after specific contact time, the adsorbent is collected magnetically and the supernatant is diluted appropriately for measurement of Cr(VI) concentration. Typically, 3 mL of the solution is mixed with 0.2 mL 1,5-diphenylcarbazide solution and 0.1 mL of diluted H_3PO_4. The final mixture is allowed to stand for 10 min to develop color complex (red-purple) and then its absorbance is measured by UV–vis spectrophotometer at 540 nm [4,26].

2.5. Regeneration and reusability

To study the regeneration and reusability of the adsorbent, the amount of adsorption capacity of Cr(VI) was investigated in five consecutive adsorption/desorption cycles. The desorption of Cr(VI) from loaded adsorbent was performed by 15 mL of 0.1 M NaOH. The regenerated adsorbent was washed several times by deionized water to neutralize and dried at 100 °C for 24 h and then it was used in the next cycle.

3. Results and discussion

3.1. Characterization of the adsorbent

3.1.1. XRD

The wide-angle XRD of A-M-S-MNPs is shown in Fig. 1. The strong diffraction peaks ($2\theta = 30.2, 35.5, 431, 53.5, 57, 62.6°$) are indexed to Miller indices 220, 311, 400, 422, 511, and 440, respectively. These peaks are matched with the standard Fe_3O_4 powder diffraction data (JCPDS, card 19-0629). The position and relative intensity of all diffraction peaks are in accordance with the characteristic peaks of the face centered cubic magnetite structure. The crystal size (D_{XRD}) by the Scherrer's equation ($D_{XRD} = K\lambda/\beta Cos\theta$) at diffraction peak ($2\theta = 35.5°$) was obtained 90 nm.

To confirm the mesoporous structure, the samples were examined by small angle X-ray diffraction (SA-XRD) as shown in Fig. 2.

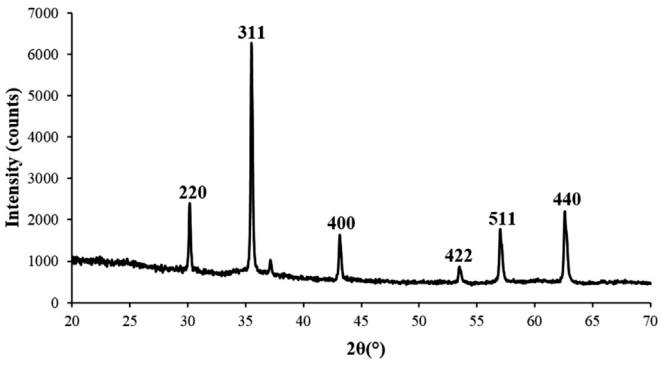

Fig. 1. The wide-angle XRD pattern of A-M-S-MNPs.

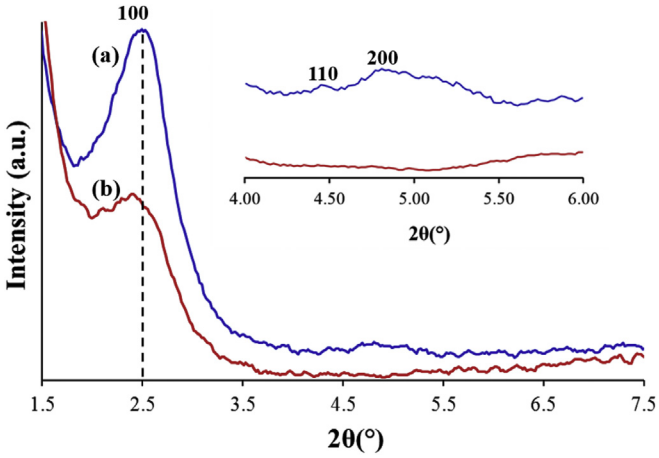

Fig. 2. The SA-XRD spectra of (a) the M-S-MNPs and (b) A-M-S-MNP.

The M-S-MNPs show a typical mesoporous structure with three characteristic peaks corresponding to (100), (110) and (200) planes. After grafting of APTES molecules, the intensity of (100) XRD peak decreases and higher order diffraction peaks (110 and 200) do not observe. This attributed to filling the pores of mesoporous structure by APTES molecules that decrease order of the mesoporous structure. In addition, the shift of (100) XRD peak to smaller angle in the SA-XRD pattern of A-M-S-MNPs is due to the expansion in unite cell after covalent linkage of aminosilane molecules on ordered mesoporous structure [27] (see Table 1a.).

3.1.2. FTIR spectra

The FTIR spectra of MNPs, S-MNPs, C-S-MNPs, M-S-MNPs and A-M-S-MNPs are displayed in Fig. 3. All of them have a peak around 580 cm^{-1} that accordance with Fe–O vibration band from magnetite phase. In the case of S-MNPS sample (Fig. 3; (b)), there are typical vibration bands of SiO_2, including Si–O–Si bending at 468 cm^{-1}, Si–O–Si symmetric stretching at 803 cm^{-1}, Si–O–H stretching vibration at 953 cm^{-1}, and Si–O–Si asymmetric stretching at 1090 and 1233 cm^{-1}. Additionally, the broad peak in the range 3200–3750 cm^{-1} and the band at 1640 cm^{-1} are related to OH groups in silanol groups and adsorbed water molecules. These characteristic peaks are also observed in other samples (Fig. 3; (c–f)). For C-S-MNPs, three peaks at 1487, 2848 and 2917 cm^{-1} are attributed to bending, symmetric and asymmetric

Table 1
a. The 2θ,d-spacing of plane (100) and unit cell parameter a_0 for M-S-MNPs and A-M-S-MNP. b. The elemental analysis and APTES group content in mmol g^{-1} by three different methods.

Table 1a

Sample	2θ (100)	2θ (110)	2θ (200)	d_{100} (nm)	a_0 (nm)
M-S-MNPs	2.50	4.42	4.81	3.58	4.13
A-M-S-MNPs	2.39	–	–	3.73	4.31

Table 1b

Sample	Elemental analysis (wt.)%			APTES loading[a] (mmol/g)	APTES loading[b] (mmol/g)		APTES loading[c] (mmol/g)
	C	H	N		H	NH	
A-M-S-MNPs	5.31	1.18	0.40	0.28	0.38	0.26	0.20

[a] Calculated from the elemental analysis data.
[b] Calculated from the TGA data, H and NH represent full and non-hydrolyzed forms of grafted APTES respectively.
[c] Measured by imine formation.

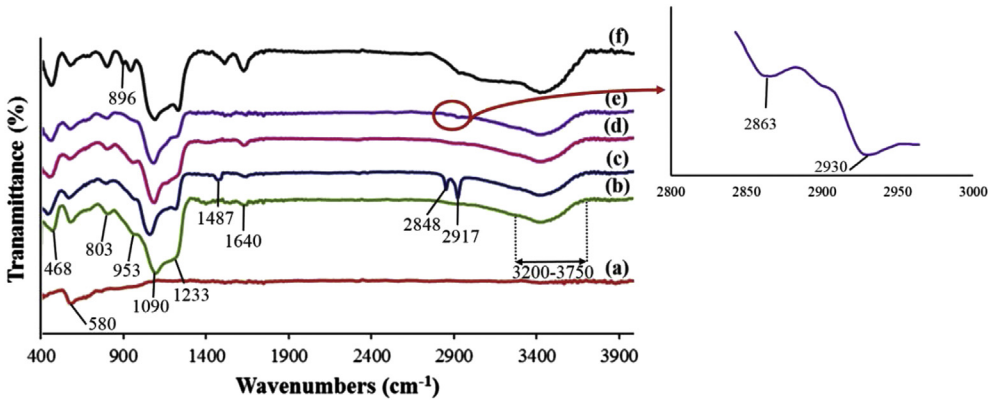

Fig. 3. FTIR spectra of (a) MNPs, (b) S-MNPs, (c) C-S-MNPs, (d) M-S-MNPs, (e) A-M-S-MNPs and (f) Cr(VI)-A-M-S-MNPs. The inset enlarges the wavenumber range 2800 cm^{-1}-3000 cm^{-1} for A-M-S-MNPs.

stretching vibration of $-CH_2-$ of CTAB template, respectively. After solvent extraction, no adsorption peaks were observed in the range of 2800–3000 cm^{-1} for M-S-MNPs that indicate the effective removal of CTAB templates. Due to overlapping of the $-NH_2$ bending and stretching vibrations with vibrations attributed to OH group in grafting APTES molecules on the surface of A-M-S-MNPs confirm by two peaks at 2863 and 2930 cm^{-1}. These peaks could be related to symmetric and asymmetric stretching modes of the $-CH_2$ of aminopropyl groups, respectively [28]. After adsorption of Cr(VI) on A-M-S-MNPs, a new peak at 896 cm^{-1} arises from Cr=O or Cr–O vibration of loaded Cr(VI) specie in Cr(VI)-A-M-S-MNPs [29].

3.1.3. TEM analysis

The morphology of the prepared A-M-S-MNPs was examined by TEM image. Fig. 4 shows that the A-M-S-MNPs are slightly irregular in shape and seem approximately spherical. Diameter of these nanoparticles are estimated about 150–200 nm. In addition, the mesoporous silica layer coated the core with some variation in shell thickness is about 25 nm. The polymerization of grafted aminopropyl groups on the surface of A-M-S-MNPs by silanization reaction leads to the attachment of their mesoporous silica layer together.

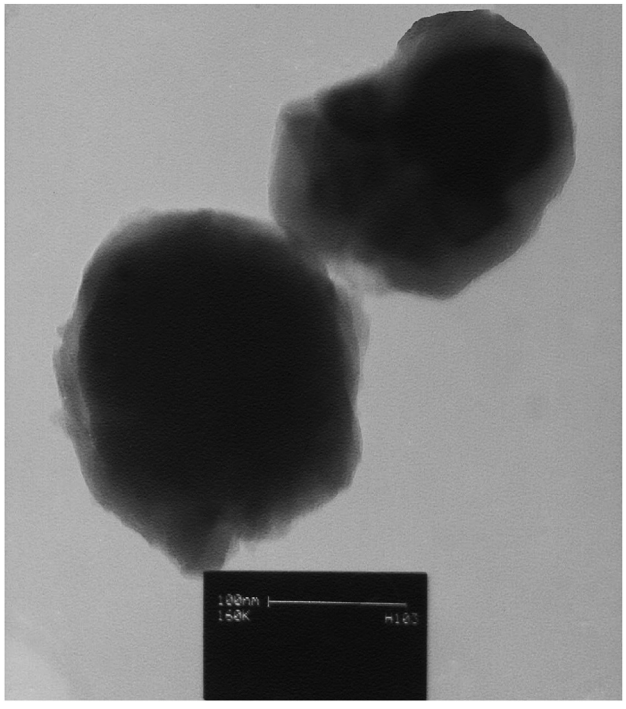

Fig. 4. TEM image of A-M-S-MNPs.

3.1.4. EDX spectrum

The EDX was used to analyze the elemental constituents of A-M-S-MNPs (Fig. 5). By applying acceleration voltage of 20 kV the K-level emission lines of Fe ($K_\alpha = 6.41$ and $K_\beta = 7.06$ keV) are identified at high energies. The energy range below 2.5 keV where the K_α emission lines of C, O and Si are observed at 0.28, 0.52, and 1.74 keV, respectively. The L-lines of Fe (0.70 keV) are also located in this energy range. These emission lines are confirmed the synthesis of Fe_3O_4 nanoparticles that are embedded in silica shells. Also the C peak is a direct evidence of attachment of APTES molecules to the nanocomposite surface that arises from propyl and ethoxy groups in APTES molecules. The N emission line (0.39 keV) that is related to the amine group ($-NH_2$) in anchored APTES was not detected at high acceleration voltage of 20 kV. For observation of this peak, the acceleration voltage was reduced to 5 kV (inset picture of Fig. 5).

3.1.5. TGA/DTA analysis

The TGA/DTA curve of A-M-S-MNPs (Fig. 6) shows three weight loss peaks. The first peak (43 °C) can be attributed to the desorption of water molecules from the surface of the silica layer. The decomposition of attached APTES molecules occurs at 342 °C and the last weight loss peak at 466 °C is accordance with the removal of surfactant [30]. The temperature for breakdown of grafted APTES groups is much higher than the boiling point of the pure APTES at 217 °C. The results imply that the APTES molecules are bonded chemically (siloxane bond) to the surface of A-M-S-MNPs and exhibit a relatively high thermal stability [31]. The amount of weight loss (5.1 wt.%) at 342 °C was used to determine the amount of APTES loading in A-M-S-MNPs. For this purpose, it was assumed that full and non-hydrolyzed forms of grafted APTES molecules were decomposed through siloxane bond (Si–O–Si) cleavage. The obtained results were listed in Table 1b.

3.1.6. Elemental analysis

Further investigation was carried out on the functionalized sample by elemental analysis. The obtained contents of nitrogen, carbon and hydrogen from this method are reported in Table 1b, which suggest a coverage of aminopropyl groups on the surface of

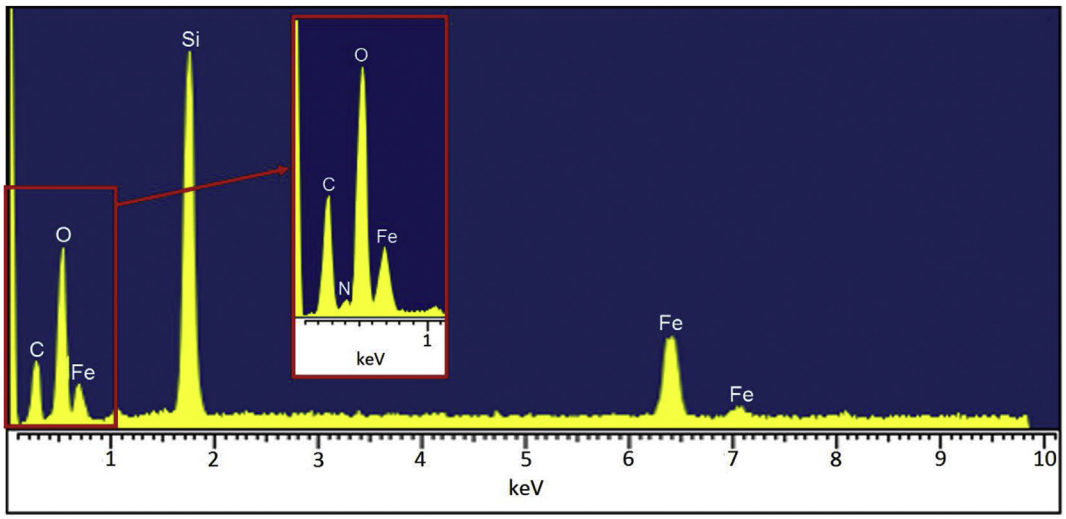

Fig. 5. EDX spectrum of the A-M-S-MNPs at 20 kV acceleration voltage. The N peak (0.39 keV) in inset picture is appeared at acceleration voltage of 5 kV.

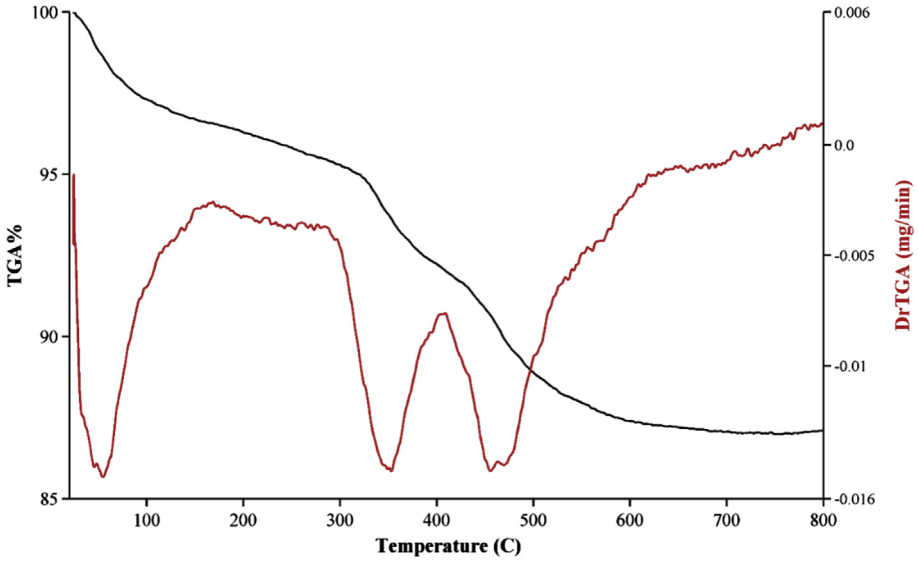

Fig. 6. TGA/DTA curve of A-M-S-MNPs.

A-M-S-MNPs. Based on elemental analysis, the loading of APTES was calculated 0.28 mmol g^{-1}.

3.1.7. Imine formation

The total amount of amine groups was measured by a surface imine reaction. In this method, 4-nitrobenzaldehyde molecules (UV sensitive) react with amine groups under argon atmosphere and generate imine groups. This reaction can be returned toward producing precursors in the presence of a certain amount of water (Scheme 1). The regenerated 4-nitrobenzaldehyde concentration are determined spectrophotometrically at $\lambda = 282$ nm that is proportional to the numbers of reacted amine groups. The experimental procedure is consistent with the works that has been done already [32]. Typically, 0.01 g of A-M-S-MNPs was placed in a capped vial and was sonicated in an ultrasonic bath four times with 2 mL of acetic acid solution (0.08% v/v) in absolute ethanol. Next, 2 mL of 4-nitrobenzaldehyde solution (0.007 g in 10 mL of 0.08% acetic acid solution) was added to the suspension and allowed to react at 50 °C for 3 h. After removal of the supernatant, the nanoparticles were washed with absolute ethanol and sonicated for 2 min. In the hydrolysis step, the nanoparticles were immersed in 2 mL of acetic acid solution (0.2% v/v) in water and then mixture was stirred at 30 °C for 1 h. The hydrolyzed solution was separated from the nanoparticles with a magnet and the absorbance of regenerated 4-nitrobenzaldehyde measured at 282 nm. The concentration of this UV sensitive material in supernatant solution was calculated by the extinction coefficient (ε_{max}) that was 1.45×10^4 M^{-1} cm^{-1} in 0.2% acetic acid [33].

Based on the results in Table 1b, there is a good relation between obtained values of APTES loading from imine formation and TGA data for the non-hydrolyzed (NH) form. These values are comparable with the detected APTES by elemental analysis method and confirms that in our synthetic conditions the grafted APTES molecules are dominantly as non-hydrolyzed form.

3.1.8. Ninhydrin test

For more confirmation of the presence of amine groups on A-M-S-MNPs, the ninhydrin test was performed as reported previously [34]. At first, the un-reacted APTES molecules on the surface of A-M-S-MNPs were removed by washing with ethanol. Afterward,

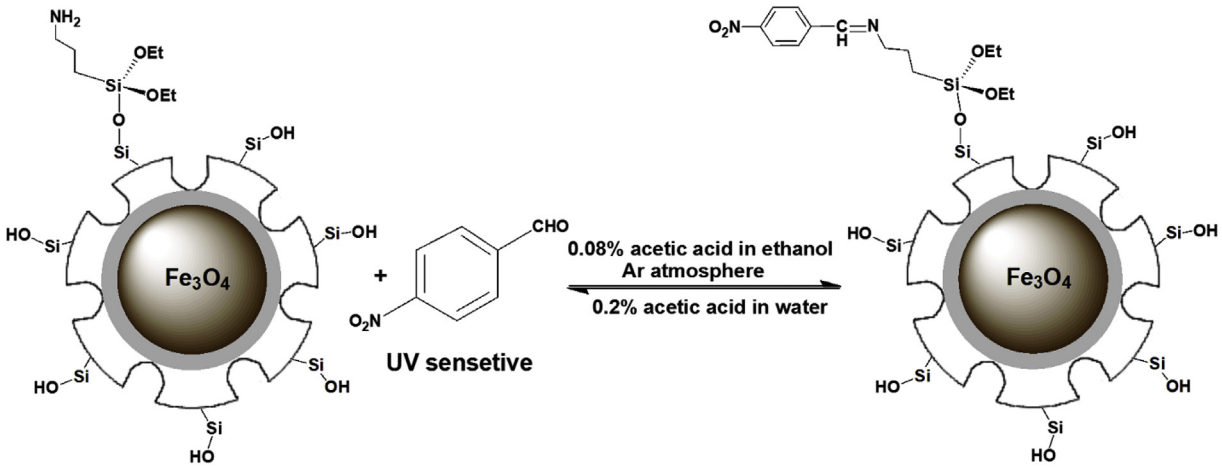

Scheme 1. Imine formation between the surface amine groups on A-M-S-MNPs and 4-nitrobenzaldehyde.

0.032 g of the washed nanoparticles was mixed with 5 mL of 0.175 M ninhydrin solution in absolute ethanol. The mixture was sonicated for 40 min and was stirred at 90 °C. After cooling to room temperature, the mixture was centrifuged and the absorbance of the generated purple–blue complex in the supernatant was determined spectrophotometrically at 588 nm [35].

3.2. Pollutants removal

3.2.1. Effect of pH

Fig. 7 is shown the effect of solution pH on the amount of Cr(VI) removal. Maximum Cr(VI) adsorption occurs when the solution pH is 2. At this pH level, which is lower than $pH_{pzc} = 7.1$ (is obtained by drift method), amino groups on the surface of adsorbent are protonated. For the Cr(VI) ion, five main species exist according to the following reactions. Based on these reactions, it can be calculated that under our condition (pH = 2) the dominate form of Cr(VI) is $HCrO_4^-$ ion [36].

$$\begin{aligned} &H_2CrO_4 \rightleftharpoons HCrO_4^- + H^+ && K_1 = 1.58 \times 10^{-1} \\ &HCrO_4^- \rightleftharpoons CrO_4^{-2} + H^+ && K_2 = 3.16 \times 10^{-7} \\ &2HCrO_4^- \rightleftharpoons Cr_2O_7^{-2} + H_2O && K_3 = 3.13 \times 10 \\ &HCr_2O_7^- \rightleftharpoons Cr_2O_7^{-2} + H^+ && K_4 = 1.17 \end{aligned} \quad (2)$$

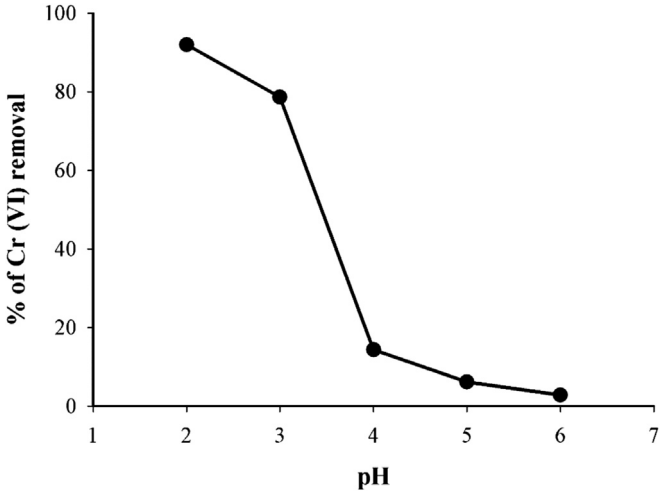

Fig. 7. Effect of pH on adsorption of Cr(VI) onto A-M-S-MNPs at 298 K. Initial concentration of Cr(VI) was 20 mg/L.

Therefore, the better adsorption of A-M-S-MNPs at pH 2 can be attributed to an electrostatic interaction between $HCrO_4^-$ and the protonated amino groups ($-NH_3^+$) on the adsorbent surface (Reaction 1).

$$\begin{aligned} &Fe_3O_4@nSiO_2@mSi-O-Si(OEt)_2Pr-NH_3^+ \\ &+ HCrO_4^- \rightleftarrows Fe_3O_4@nSiO_2@mSi-O-Si(OEt)_2Pr \\ &- NH_3^+ \ldots O_4^-Cr-H \end{aligned} \quad (1)$$

In the Reaction (1), $Fe_3O_4@nSiO_2@mSi-O-Si(OEt)_2Pr-NH_3^+$ has shown the protonated A-M-S-MNPs, and $HCrO_4^-$ as the dominate form of Cr(VI), respectively.

Since at pH values higher than 3, the $-NH_2$ groups could not be protonated completely and therefore the amount of Cr(VI) removal was decreased. As a result, Cr(VI) adsorption is related to its ionic forms in solution and the surface characteristics of the adsorbent that could be controlled by solution pH. Since low pH condition is observed for many industrial waste water, using of such pH as an optimum media for removal of Cr(VI) is realistic.

Furthermore, the DFT study of Cr(VI) adsorption in acidic condition shows that hydrogen bonds between $HCrO_4^-$ and functional groups on the adsorbent surface ($-NH_3^+$ and surface Si–OH groups) play an important role in the adsorption process.

3.2.2. Effect of Cr(VI) concentration and contact time

In order to evaluate the adsorption efficiency of Cr(VI) on the surface of A-M-S-MNPs with time, three solutions were prepared at different concentrations (20, 30 and 50 mg/L). Fig. 8 shows that A-M-S-MNPs is a very effective adsorbent in removing of Cr(VI) within 30 min. The rapid decrease of Cr(VI) concentration within initial times attributed to high concentration of surface $-NH_3^+$ groups and strong interaction between $HCrO_4^-$ and adsorbent. The results also show that the reduction of concentration leads to lower adsorption of Cr(VI) on adsorbent surface at more than 30 min.

3.2.3. Adsorption kinetic

To study the adsorption kinetics of Cr(VI), pseudo first-order and pseudo second-order equations were used. The Eqs. (3) and (4) describe these kinetic models, respectively.

$$\log(q_e - q_t) = \log q_e - \frac{k_1}{2.303}t \quad (3)$$

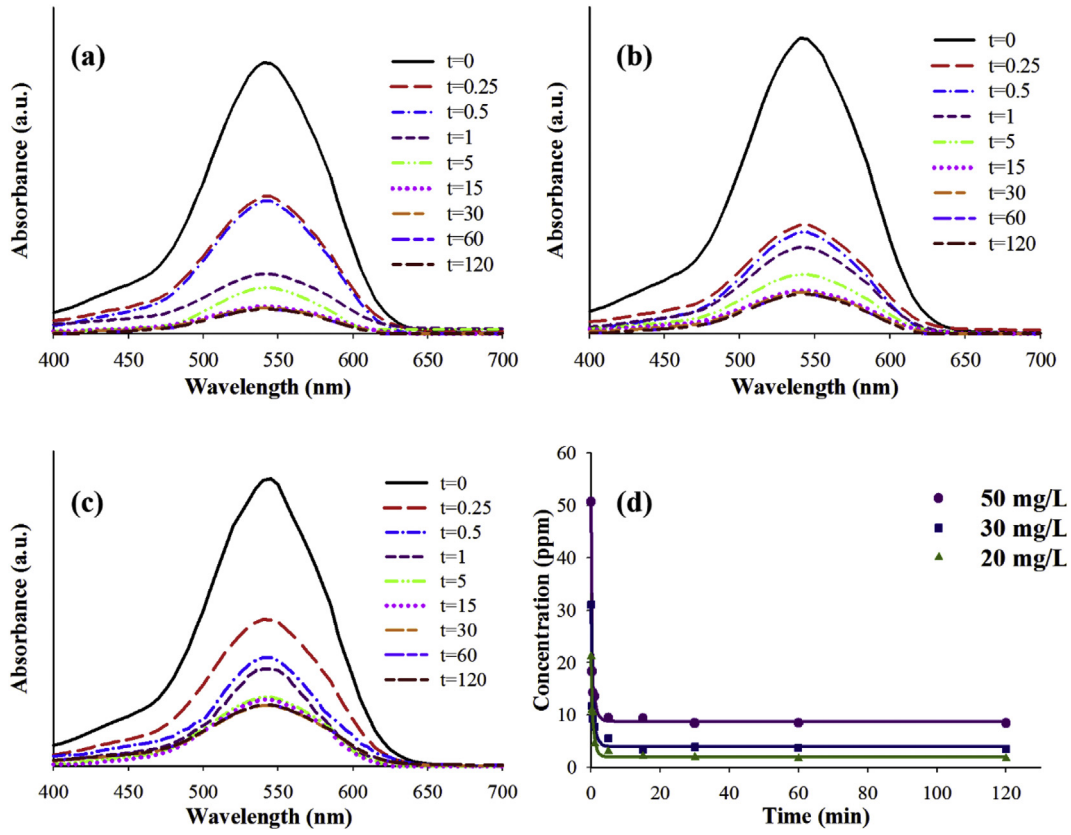

Fig. 8. UV–vis curves of changes of Cr(VI) concentration for (a) 20 mg/L solution, (b) 30 mg/L solution and (c) 50 mg/L solution during 120 min. (d) comparison of the removal efficiency of Cr(VI) in these solutions during 120 min and pH 2.

$$\frac{t}{q_t} = \frac{1}{k_2 q_e^2} + \left(\frac{1}{q_e}\right) t \tag{4}$$

where q_e is the amount of adsorbed Cr(VI) at equilibrium (mg/g), q_t is the amount of Cr(VI) adsorbed on A-M-S-MNPS at time t (mg/g), k_1 (min^{-1}) is the pseudo-first-order rate constant and k_2 (g mg^{-1} min^{-1}) is the pseudo-second-order rate constant of adsorption.

The adsorption kinetics were studied for different solutions 20, 30 and 50 mg/L. Based on Fig. A.1 and correlation coefficients in Table 2, the kinetics for the removal of Cr(VI) fitted well with the pseudo-second order model. It means that in addition of $-NH_3^+$ groups, the surface silanols can interact with $HCrO_4^-$ ions too [37]. Another cause for the further confirmation of pseudo-second order kinetic model for adsorption Cr(VI) onto A-M-S-MNPs is related to the match of calculated q_e values, $q_{e,cal}$, with experimental data. The

Table 2
Kinetic parameters for the adsorption of Cr(VI) onto A-M-S-MNPs at 298 K.

Concentration (mg/L)	Pseudo-second order			
	k_2 (g/mg min)	$q_{e,cal}$ (mg/g)	$q_{e,exp}$ (mg/g)	R^2
20	0.271 (±0.005)	13.947 (±0.154)	13.905 (±0.118)	0.999
30	0.240 (±0.008)	19.724 (±0.226)	19.722 (±0.122)	0.999
50	0.211 (±0.007)	30.211 (±0.360)	30.207 (±0.036)	0.999

Concentration (mg/L)	Intraparticle diffusion		
	k_i (mg/g $min^{0.5}$)	c	R^2
30	2.102 (±0.030)	13.631 (±0.055)	0.985
50	2.820 (±0.071)	23.233 (±0.115)	0.980

k_2 values indicate that it decreases from 0.271 to 0.211 g/mg min as initial concentration increases from 20 to 50 mg/L (Table 2). This inverse relationship was observed by other researches [6].

Adsorption is a three-step process consist of transport of adsorbate molecules solution to the external surface of the adsorbent (film diffusion or boundary layer diffusion), diffusion of the adsorbate into the pores of the adsorbent and adsorption of the adsorbate on the internal of adsorbent. Since adsorption step is very fast, the rate-controlling step in adsorption processes is the first two steps or combination of both steps. For the intraparticle diffusion rate equation is given by:

$$q_t = k_i t^{0.5} + c \tag{5}$$

where k_i is the intra-particle diffusion rate constant (mg/g $min^{0.5}$) and c is the intercept. The k_i value can be calculated from the slope of plot of q_t versus $t^{0.5}$.

Time dependence of q_t for three different concentrations are represented in Fig. A.1c. In 20 mg/L solution, this dependency displays a two-part curve, which confirms two distinct kinetic regions; film diffusion and adsorption. But the story for 30 and 50 mg/L solutions are different such that increasing of concentration of Cr(VI) ion leads to three-part curves for these solutions. As is clear, a new section appears between film diffusion and adsorption steps that is related to intraparticle diffusion. It seems that this disparity comes from different adsorption mechanisms in low and high concentrations. In low concentrations, the film diffusion is the rate determining step of adsorption process while in high concentrations, the rate determining step changes. Since the second part of the curve in concentrations of 30 and 50 mg/L did not pass through the origin ($c \neq 0$), it is concluded that not only intraparticle

diffusion is rate-controlling step but also the film diffusion limits adsorption process to some extent. The intraparticle diffusion rate constants are obtained from the slope of the second portion of curves in Fig. A.1c and are reported in Table 2. The results shows that k_i value for 50 mg/L is the greater than 30 mg/L. It can be explained by change of driving force of with concentration of adsorbate in bulk solution. The increase of Cr(VI) concentration leads to increase of driving force and it increases diffusion rate of $HCrO_4^-$ ions into the pores of the substrate. The obtained c values is proportional to the thickness of the boundary layer, i.e., the larger the intercept, the greater the boundary layer effect [38].

3.2.4. Effect of ionic strength

The effect of ionic strength (KNO_3 and NaCl) on adsorption of Cr(VI) was studied at optimum pH. Fig. A.2 shows that the extent of Cr(VI) adsorption decreased with increasing of ionic strength from 10^{-5} to 10^{-1} M. As it was discussed in pH effect, attractive electrostatic forces and hydrogen bonds between the adsorbent and $HCrO_4^-$ ions are effective factors in adsorption. The ionic strength could decline the attractive forces by two ways: 1) neutralizing the negative charge of $HCrO_4^-$ and 2) occupying positively adsorption sites ($-NH_3^+$) [39]. In addition, charge reduction of adsorbate and adsorbent decreases electron sharing and weakens the formed hydrogen bonds. Therefore, the salts with decreasing attractive forces and hydrogen bond strength significantly reduces the adsorption Cr(VI) on A-M-S-MNPs.

3.2.5. Adsorption isotherm model

To evaluate the adsorption process of Cr(VI) onto A-M-S-MNPs, the well-known Langmuir and Freundlich adsorption isotherm models were used to simulate experimental data. The linear form of the Langmuir isotherm can be represented by the following equation:

$$\frac{1}{q_e} = \frac{1}{q_m} + \frac{1}{bq_mC_e} \tag{6}$$

where q_e is the amount of adsorbate on adsorbent at equilibrium (mg/g), C_e (mg/L) is the equilibrium concentration of adsorbate, q_m (mg/g) is the maximum adsorption capacity and b (L/mg) is the Langmuir adsorption equilibrium constant. The values of b and q_m were calculated from the slope and intercept of plot of $1/q_e$ versus $1/C_e$, respectively.

The Freundlich isotherm model can be depicted by the following equation:

$$logq_e = logK_f + \frac{1}{n}logC_e \tag{7}$$

where K_f indicates the adsorption capacity and n is heterogeneity factor which for a favorable adsorption is larger than one ($n > 1$). The values of K_f and n can be obtained from the plotting of log q_e versus log C_e.

The parameters of the Langmuir and Freundlich isotherm models are listed in Table 3. The high values of the correlation coefficients confirm that Langmuir isotherm fits the obtained data better than Freundlich model. It means that an uniform and monomolecular adsorption occurs on the A-M-S-MNPs. The results also show that the q_m values increase from 33 to 50 mg/g with 20 °C increasing in temperature. This indicates that the adsorption capacity of A-M-S-MNPs is extremely dependent to the temperature changes. The temperature dependency seems to come from conformational changes of functional groups on the nanoparticle surface. By heating, the rotational energy of functional groups increases and leads to destroy some of the hydrogen bonds between them. The $-NH_3^+$ groups, as adsorption sites, become more available and their adsorption ability are increased. Furthermore, access to the adsorption sites inside pores becomes easier because of surface hydrogen bonds destruction (Scheme 2).

3.2.6. Thermodynamic parameters

The change in free energy ΔG^0, enthalpy ΔH^0 and entropy ΔS^0 of adsorption can be obtained from the temperature dependence of adsorption isotherms. The following equations are used for the determination of the values of these thermodynamic parameters.

$$\left.\begin{aligned}\Delta G^0 &= -RTlnK\\ \Delta G^0 &= \Delta H^o - T\Delta S\end{aligned}\right\} \Rightarrow lnK = \frac{\Delta S^0}{R} - \frac{\Delta H^0}{RT} \tag{8}$$

The values of ΔH^0 and ΔS^0 were obtained from the slope and intercept of a plot of lnK versus 1/T at different temperatures. The positive value of ΔH^0 confirms that the adsorption of Cr(VI) ions is an endothermic process. The negative values of ΔG^0 for the adsorption of Cr(VI) indicate that the adsorption is a spontaneous process (see Table 4). The positive value of ΔS^0 reflects the tendency of A-M-S-MNPs toward Cr(VI) ions in aqueous solutions and propose some structure changes in the adsorbent.

3.2.7. Regeneration and reusability

In order to evaluate the regeneration of A-M-S-MNPs, the desorption of Cr(VI) from adsorbate surface was performed by different NaOH solutions (0.01–0.1 M). The results show that the desorption efficiency can reach to 97% when the concentration of NaOH solution is 0.1 M. The mechanism of desorption under basic condition can be explained by the deprotonation of attached $-NH_3^+$ groups on the adsorbent surface (Reaction 2). Due to the formation of $-NH_2$ groups on the surface, the electrostatic interaction between these groups and $HCrO_4^-$ decreases and leads to the desorption process. Furthermore, this causes a decrease of the hydrogen bond power due to the less tendency of $-NH_2$ groups to form hydrogen bond. Since adsorption and regeneration process occur at low and high pH values, a pH swing adsorption is observed.

$$\begin{aligned}&Fe_3O_4@nSiO_2@mSi-O-Si(OEt)_2Pr-NH_3^+\\ &+OH^- \rightleftarrows Fe_3O_4@nSiO_2@mSi-O-Si(OEt)_2Pr-NH_2+H_2O\end{aligned} \tag{2}$$

As shown in Fig. 9, the adsorption capacity of Cr(VI) is about 30.2 (mg/g) in the first cycle and decreases to 24.5 (mg/g) in the fifth cycle. It assumes that this behavior comes from the mesoporous channels which are blocked with some $HCrO_4^-$ ions in each cycle and decreases the adsorption capacity in the next cycles.

Comparison of our results with commercial adsorbents such as modified zeolites and activated carbon shows that A-M-S-MNPs have many advantages. A very high adsorption capacity is observed for our modified adsorbent with respect to the literatures [40–42]. A-M-S-MNPs could be separated easily from aqueous solutions due to having magnetic properties. In addition, the regeneration of this adsorbent take places at ambient temperature despite of activated

Table 3
Isotherm parameters of Langmuir and Freundlich models for the adsorption of Cr(VI) at different temperatures.

T (K)	Langmuir			Freundlich		
	q_m (mg/g)	b (L/mg)	R^2	K_f	n	R^2
298	34.25	0.25	0.99	19.11	8.15	0.94
308	45.25	0.27	0.99	23.94	7.19	0.94
318	50.51	0.30	0.98	27.09	7.09	0.97

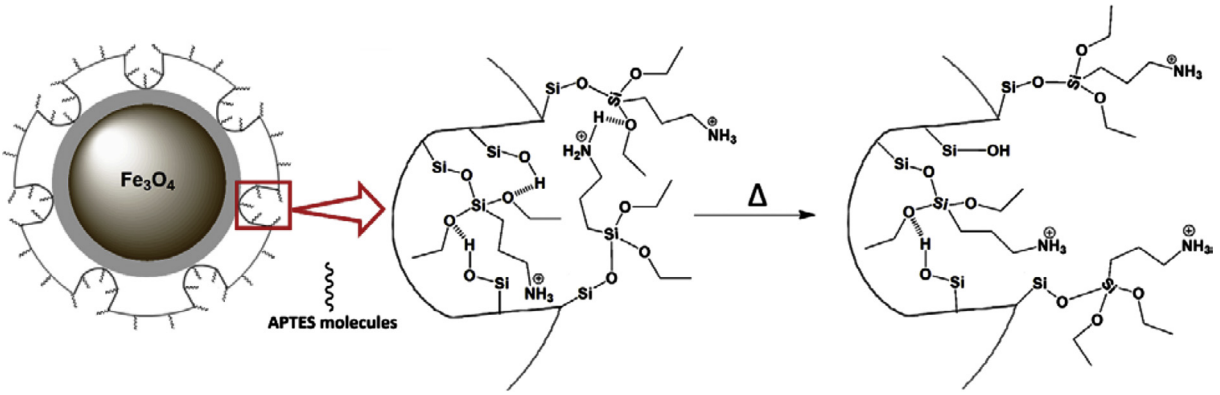

Scheme 2. Conformational changes of surface functional groups of A-M-S-MNPs with increasing temperature. This increases the q_m of the adsorbent.

Table 4
Thermodynamic parameters of Cr(VI) adsorption on A-M-S-MNPs at different temperatures.

T (K)	lnK	ΔG^0 (kJ mol^{-1})	ΔH^0 (kJ mol^{-1})	ΔS^0 (J mol^{-1} k^{-1})
298	13.96 (±0.04)	−34.60± (0.23)	8.25± (0.41)	143.66± (1.17)
308	14.04 (±0.02)	−35.98± (0.21)		
318	14.17 (±0.01)	−37.47± (0.13)		

carbon [43]. All of these advantages make A-M-S-MNPs as a better adsorbent than commercial ones.

3.3. Theoretical adsorption energies

Furthermore, the adsorption of Cr(VI) on the different amino-functionalized silica surfaces was modeled by DFT calculations. For this purpose the adsorption of Cr(VI) on amino-functionalized silica surfaces were performed by using ONIOM methodology that is implied in Gaussian 09 program package [44]. In our previous study, we designed 16 different configurations for amino-functionalized silica surfaces and they were classified in five categories [45]. In this study, the most stable configurations of each group were considered for investigation of adsorption of $HCrO_4^-$ on amino-functionalized silica surfaces. To simplify, the selected surfaces were named based on the name of their categories, for example, 3-ethoxy4 changed to 3-ethoxy. Given that the adsorption of $HCrO_4^-$ molecules onto amino-functionalized silica surfaces occurs in acidic environment, $-NH_2$ groups in two attached APTES molecules were protonated and changed to $-NH_3^+$. For study of adsorption processes two optimized $HCrO_4^-$ molecules were placed on top of each designed surfaces and then the surface—$HCrO_4^-$ complexes were optimized. In addition, for increasing the accuracy of calculations of adsorption energies, the single point energy calculations were performed at high level of theory. Furthermore, the Conductor-like Polarizable Continuum Model (CPCM, solvent = water) was used for solvation effects [46,47].

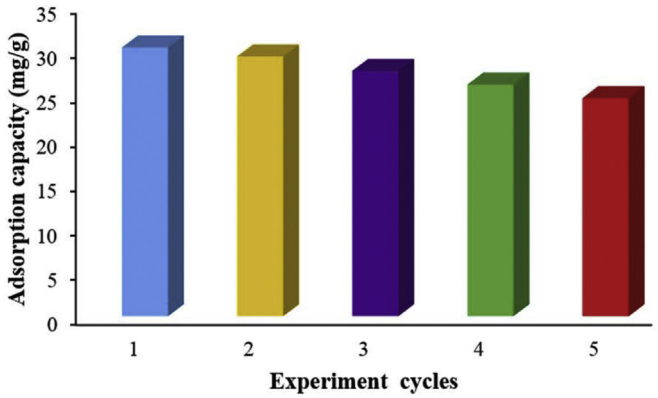

Fig. 9. Reusability of the A-M-S-MNPs during five adsorption/desorption cycles.

The adsorption energies were calculated using the following equation:

$$Adsorption\ energy = -\left[E_{surface\cdots HCrO_4^-} - \left(E_{surface} + 2E_{HCrO_4^-}\right)\right]$$

where $E_{surface\cdots HCrO_4^-}$ refers to the total energy of two $HCrO_4^-$ molecules on the surface while $E_{surface}$ and $E_{HCrO_4^-}$ are taken as the energies of surface without the $HCrO_4^-$ molecule and the $HCrO_4^-$ molecule, respectively.

Based on our calculation, the adsorption energy per $HCrO_4^-$ ion on the 4-ethoxy surface is 9.42 kJ mol^{-1} while this value increases to 26.61, 44.60, 55.64, and 37.01 kJ mol^{-1} from 3-ethoxy to 0-ethoxy surfaces, respectively. The obtained results indicate that the experimental adsorption energy ($\Delta H = 8.25$ kJ mol^{-1}) is similar to the theoretical value for the modeled 4-ethoxy surface. This result is accordance with outcomes from TGA, elemental analysis and imine reaction, which the grafted APTES molecules are dominantly as the non-hydrolyzed form.

Since the basis set super position error (BSSE) could affect the amount of calculated adsorption energies, its determination is important in accuracy of the obtained results [48]. Unfortunately, BSSE calculation with ONIOM method in solvation media is not possible in Gaussian program. Therefore, an approximation method was used to estimate BSSE corrections. The BSSE corrections were computed for QM level in the gas phase for surface—$HCrO_4^-$ complexes to understand the accuracy of our applied basis set. Since the calculated BSSE corrections were calculated for QM level in gas phase, they could not add to the adsorption energy values and only are used for the estimation of the super position error of applied basis set. Analysis of the BSSE correction values for 4-ethoxy to 0-ethoxy surfaces locates in the range of 2.1–3.5 kJ mol^{-1}, respectively. This range indicates that our selected basis set is suitable and its super position error is negligible.

In addition, the nature of surface interactions was examined from these designed models. It was guessed that the electrostatic and hydrogen bond interactions play important role in the adsorption process. Charge distribution shows that the electrostatic attractions occurs between positive $-NH_3^+$ and negative $HCrO_4^-$ groups. This is while the bond length analysis determines the —N—H···O—Cr and —O—H···O—Cr hydrogen bonds interactions

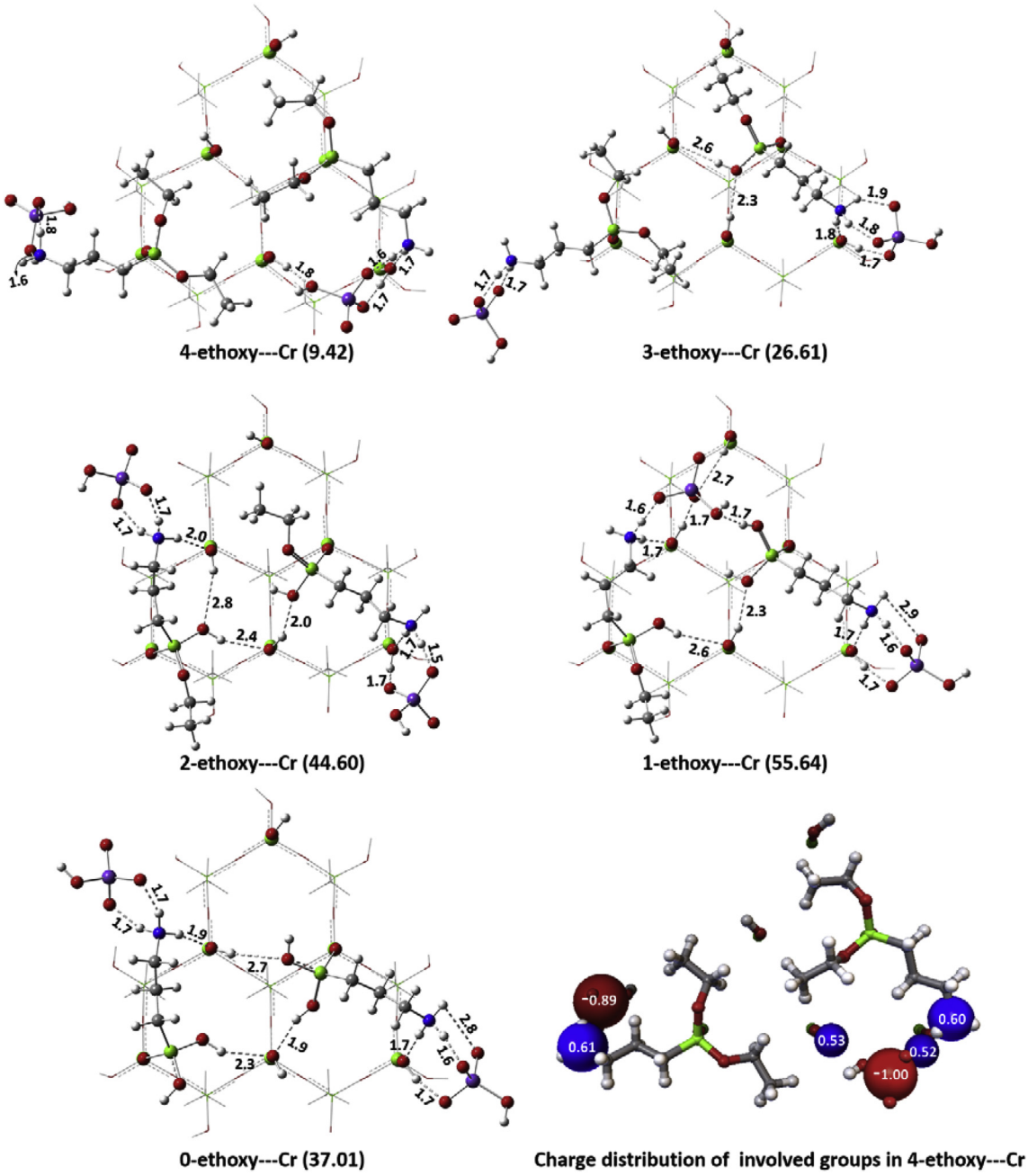

Fig. 10. Adsorption of Cr(VI) ion on different amino-functionalized silica surfaces in acidic condition. Adsorption energies in kJ mol^{-1} are given below each surface in parentheses. The oxygen, carbon, silicon, chromium and hydrogen atoms are shown as red, gray, green, purple and white colors, respectively. The electrostatic interactions are also clear from charge distribution of involved groups in 4-ethoxy—Cr complex. (For interpretation of the references to colour in this figure legend, the reader is referred to the web version of this article.)

between adsorbent and adsorbates (Fig. 10). Formation of these hydrogen bonds between $HCrO_4^-$ ion and surface functional groups confirms our results about pseudo-second order kinetic model that in addition of $-NH_3^+$ groups, the surface silanols can be as adsorption site.

4. Conclusions

In summary, A-M-S-MNPs as a novel magnetic sorbent with a mesoporous shell has been synthesized using APTES as the surface modification agent. XRD, FTIR spectrum, TEM, EDX, elemental analysis, TGA/DTA techniques were used for the chemical and structural characterization of the adsorbent. Furthermore, the imine reaction and ninhydrin test were applied to confirm that the grafted APTES molecules on the surface. Comparison between the amount of APTES loading from three methods TGA/DTA, elemental analysis and the imine reaction showed that the grafted APTES molecules exist predominantly as their non-hydrolyzed form. High adsorption capacity (34.25 mg/g at 298 K) for Cr(VI) removal at pH = 2 refers to a favorable degree of site-isolation of the functional groups (the distance between the two or more functional groups). In lower distance, intramolecular hydrogen bonds between adjacent amine groups form. This leads to blocking of the pores and decreasing of surface functional group protonation, which both of

them decline the adsorption capacity. In higher distance than optimum one, the functional groups on the surface reduces and leads to lower adsorption capacity. As a result, A-M-S-MNPs could be used as a promising adsorbent for the removal of Cr(VI) from water and acidic industrial wastewater samples. In strong acidic condition A-M-S-MNPs is stable and $-NH_3^+$ groups on surface provide suitable adsorption sites.

The quantum mechanics calculations indicate that the electrostatic attraction and hydrogen bonds are the two effective interactions in the adsorption of Cr(VI) on the adsorbent. These results were obtained from charge distribution and bond length analysis. The theoretical adsorption energies confirm our suggestion about the non-hydrolyzed surface groups.

Acknowledgments

The support of Ferdowsi University of Mashhad (Research and technology) for this work (3/21048-07/03/2012) is appreciated. The authors acknowledge from high performance computing center (HPCC) of Ferdowsi University of Mashhad, Iran (3/21048) for their assistances too.

Appendix A. Supplementary data

Supplementary data related to this article can be found at http://dx.doi.org/10.1016/j.micromeso.2015.07.008.

References

[1] V.K. Gupta, A. Rastogi, A. Nayak, J. Colloid Interface Sci. 342 (2010) 135–141.
[2] Y. Xing, X. Chen, D. Wang, Environ. Sci. Technol. 41 (2007) 1439–1443.
[3] O. Ajouyed, C. Hurel, M. Ammari, L.B. Allal, N. Marmier, J. Hazard. Mater. 174 (2010) 616–622.
[4] D. Dinda, A. Gupta, S.K. Saha, J. Mater. Chem. A 1 (2013) 11221–11228.
[5] P. O'Brien, A. Kortenkamp, Transit. Met. Chem. 20 (1995) 636–642.
[6] M. Bhaumik, A. Maity, V.V. Srinivasu, M.S. Onyango, J. Hazard. Mater. 190 (2011) 381–390.
[7] X.-F. Sun, Y. Ma, X.-W. Liu, S.-G. Wang, B.-Y. Gao, X.-M. Li, Water Res. 44 (2010) 2517–2524.
[8] M. Liu, T. Wen, X. Wu, C. Chen, J. Hu, J. Li, X. Wang, Dalton Trans. 42 (2013) 14710–14717.
[9] W. Jiang, M. Pelaez, D.D. Dionysiou, M.H. Entezari, D. Tsoutsou, K. O'Shea, Chem. Eng. J. 222 (2013) 527–533.
[10] H. Niu, D. Zhang, S. Zhang, X. Zhang, Z. Meng, Y. Cai, J. Hazard. Mater. 190 (2011) 559–565.
[11] Y.G. Zhao, H.Y. Shen, S.D. Pan, M.Q. Hu, J. Hazard. Mater. 182 (2010) 295–302.
[12] A.H. Lu, E.e.L. Salabas, F. Schüth, Chem. Int. Ed. 46 (2007) 1222–1244.
[13] D. Zhao, Q. Huo, J. Feng, B.F. Chmelka, G.D. Stucky, J. Am. Chem. Soc. 120 (1998) 6024–6036.
[14] F. Hoffmann, M. Cornelius, J. Morell, M. Fröba, Angew. Chem. Int. Ed. 45 (2006) 3216–3251.
[15] X. Zhuang, Q. Zhao, Y. Wan, J. Mater. Chem. 20 (2010) 4715–4724.
[16] M. Moritz, Appl. Surf. Sci. 283 (2013) 537–545.
[17] M. Zhu, M.Z. Lerum, W. Chen, Langmuir 28 (2011) 416–423.
[18] H. Yang, Q. Feng, Microporous Mesoporous Mater. 135 (2010) 124–130.
[19] J. Aguado, J.M. Arsuaga, A. Arencibia, M. Lindo, V. Gascón, J. Hazard. Mater. 163 (2009) 213–221.
[20] S.H. Araghi, M.H. Entezari, Appl. Surf. Sci. 333 (2015) 68–77.
[21] A. Maria Chong, X. Zhao, J. Phys. Chem. B 107 (2003) 12650–12657.
[22] H. Ritter, M. Nieminen, M. Karppinen, D. Brühwiler, Microporous Mesoporous Mater. 121 (2009) 79–83.
[23] M.A. Vergés, R. Costo, A. Roca, J. Marco, G. Goya, C. Serna, M. Morales, J. Phys. D. Appl. Phys. 41 (2008) 134003.
[24] J. Kecht, A. Schlossbauer, T. Bein, Chem. Mater. 20 (2008) 7207–7214.
[25] S. Ek, A. Root, M. Peussa, L. Niinistö, Thermochim. Acta 379 (2001) 201–212.
[26] M. Baikousi, A.B. Bourlinos, A. Douvalis, T. Bakas, D.F. Anagnostopoulos, J.i. Tucek, K.r. Safarova, R. Zboril, M.A. Karakassides, Langmuir 28 (2012) 3918–3930.
[27] A.M. Furtado, D. Barpaga, L.A. Mitchell, Y. Wang, J.B. DeCoste, G.W. Peterson, M.D. LeVan, Langmuir 28 (2012) 17450–17456.
[28] L. Song, T. Bu, L. Zhu, Y. Zhou, Y. Xiang, D. Xia, J. Phys. Chem. C 118 (2014) 9468–9476.
[29] Z. Zhu, Z. Chang, L. Kevan, J. Phys. Chem. B 103 (1999) 2680–2688.
[30] D.B. Nale, S. Rana, K. Parida, B.M. Bhanage, Catal. Sci. Tech. 4 (2014) 1608–1614.
[31] S.-C. Shen, W.K. Ng, L. Chia, Y.-C. Dong, R.B. Tan, Mater. Res. Bull. 46 (2011) 1665–1669.
[32] J.H. Moon, J.H. Kim, K.-j. Kim, T.-H. Kang, B. Kim, C.-H. Kim, J.H. Hahn, J.W. Park, Langmuir 13 (1997) 4305–4310.
[33] A. del Campo, T. Sen, J.-P. Lellouche, I.J. Bruce, J. Magn. Magn. Mater. 293 (2005) 33–40.
[34] E. Soto-Cantu, R. Cueto, J. Koch, P.S. Russo, Langmuir 28 (2012) 5562–5569.
[35] K.K. Sharma, R.P. Buckley, T. Asefa, Langmuir 24 (2008) 14306–14320.
[36] H. Shen, S. Pan, Y. Zhang, X. Huang, H. Gong, Chem. Eng. J. 183 (2012) 180–191.
[37] S.A. Idris, K.M. Alotaibi, T.A. Peshkur, P. Anderson, M. Morris, L.T. Gibson, Microporous Mesoporous Mater. 165 (2013) 99–105.
[38] T.R. Bastami, M.H. Entezari, Chem. Eng. J. 210 (2012) 510–519.
[39] A. Ip, J. Barford, G. McKay, J. Colloid Interface Sci. 337 (2009) 32–38.
[40] W. Liu, J. Zhang, C. Zhang, Y. Wang, Y. Li, Chem. Eng. J. 162 (2010) 677–684.
[41] K. Selvi, S. Pattabhi, K. Kadirvelu, Bioresour. Technol. 80 (2001) 87–89.
[42] R. Leyva-Ramos, A. Jacobo-Azuara, P. Diaz-Flores, R. Guerrero-Coronado, J. Mendoza-Barron, M. Berber-Mendoza, Colloids Surf. A Physicochem. Eng. Asp. 330 (2008) 35–41.
[43] M. Anbia, M. Lashgari, Chem. Eng. J. 150 (2009) 555–560.
[44] M. Frisch, G. Trucks, H. Schlegel, G. Scuseria, M. Robb, J. Cheeseman, G. Scalmani, V. Barone, B. Mennucci, G. Petersson, Gaussian 09, Revision B. 01, Gaussian, Inc., Wallingford, CT, 2010.
[45] S. Hozhabr Araghi, M.H. Entezari, M.S. Sadeghi Googheri, J. Mol. Graph. Modell. 59 (2015) 21–30.
[46] V. Barone, M. Cossi, J. Phys. Chem. A 102 (1998) 1995–2001.
[47] M. Cossi, N. Rega, G. Scalmani, V. Barone, J. Comput. Chem. 24 (2003) 669–681.
[48] S.A. Mian, L.C. Saha, J. Jang, L. Wang, X. Gao, S. Nagase, J. Phys. Chem. C 114 (2010) 20793–20800.